

# SPULTRA: Low-Dose CT Image Reconstruction with Joint Statistical and Learned Image Models

Siqi Ye, Saiprasad Ravishankar, *Member, IEEE*, Yong Long\*, *Member, IEEE*,  
and Jeffrey A. Fessler, *Fellow, IEEE*

**Abstract**—Low-dose CT image reconstruction has been a popular research topic in recent years. A typical reconstruction method based on post-log measurements is called penalized weighted-least squares (PWLS). Due to the underlying limitations of the post-log statistical model, the PWLS reconstruction quality is often degraded in low-dose scans. This paper investigates a shifted-Poisson (SP) model based likelihood function that uses the pre-log raw measurements that better represents the measurement statistics, together with a data-driven regularizer exploiting a Union of Learned TRANSforms (SPULTRA). Both the SP induced data-fidelity term and the regularizer in the proposed framework are nonconvex. In the proposed SPULTRA algorithm, we iteratively design quadratic surrogate functions for the SP induced data-fidelity term, and in each algorithm iteration, we efficiently solve a quadratic subproblem for updating the image, and a sparse coding and clustering subproblem that has a closed-form solution. The SPULTRA algorithm has a similar computational cost per iteration as its recent counterpart PWLS-ULTRA that uses post-log measurements, and it provides significantly better image reconstruction quality than PWLS-ULTRA, especially in low-dose scans.

**Index Terms**—Inverse problems, sparse representation, transform learning, shifted-Poisson model, nonconvex optimization, efficient algorithms, machine learning.

## I. INTRODUCTION

Recent years have witnessed the growing deployment of X-ray computed tomography (CT) in medical diagnosis. Simultaneously there has been great concern to reduce the potential risks caused by exposure to X-ray radiation. Strategies for reducing the X-ray radiation in CT include reducing the photon intensity at the X-ray source, i.e., low-dose CT (LDCT), or lowering the number of projection views obtained by the CT machine, i.e., sparse-view CT. Since CT image reconstruction with reduced radiation is challenging, many reconstruction methods have been proposed for this setting among which model-based iterative reconstruction (MBIR) is widely used [1]. Based on maximum a posteriori (MAP) estimation, MBIR approaches form a cost function that incorporates the statistical

model for the acquired measurements and the prior knowledge (model) of the images. This section first reviews some of the statistical models for CT measurements along with recent works on extracting prior knowledge about images for LDCT image reconstruction, and then presents our contributions.

### A. Background

Accurate statistical modeling of the measurements in CT scanners is challenging, especially in low-dose imaging, when the electronic noise in the data acquisition system (DAS) becomes significant [2]–[8]. Approximations of the measurement statistics can be categorized into *post-log* and *pre-log* models [9], which are detailed next.

The post-log models work on data obtained from the logarithmic transformation of the raw measurements, which is often assumed Gaussian distributed. Since the logarithmic transformation approximately linearizes the raw measurements, methods based on post-log data can readily exploit various optimization approaches and regularization designs with efficiency and convergence guarantees for this reconstruction problem [10]–[12]. The post-log methods however have a major drawback: the raw measurements may contain non-positive values on which the logarithmic transformation cannot be taken (or near-zero positive measurements whose logarithm can be very negative), particularly when the electronic noise becomes significant as compared to the photon statistical noise in low-dose cases. There are many pre-correction approaches to deal with such raw measurements. Examples of such approaches include using a statistical weight of zero for non-positive measurements [13], replacing the non-positive measurements with a small positive value [14] and filtering neighboring measurements [2]. Thibault et al. [15] proposed a recursive filter which preserves the local mean to pre-process noisy measurements, but still used a non-linear function to map all noisy measurements to strictly positive values. When pre-processing a large percentage of non-positive values for LDCT measurements, these pre-correction methods will introduce bias in the reconstructed image and can degrade image quality [9], [15]. The logarithmic transformation itself causes a positive bias in the line integrals from which the image is reconstructed [9], [16]. A typical method for reconstructing images from the post-log data is penalized weighted least squares (PWLS) [14] that optimizes an objective consisting of a weighted least squares data fidelity term and a regularization penalty. The pre-correction process and non-linear logarithmic operation create challenges in estimating the statistical weights for the PWLS methods.

This work was supported in part by the SJTU-UM Collaborative Research Program, NSFC (61501292), NIH grant U01 EB018753, ONR grant N00014-15-1-2141, DARPA Young Faculty Award D14AP00086, and ARO MURI grants W911NF-11-1-0391 and 2015-05174-05. Asterisk indicates the corresponding author.

S. Ye and Y. Long are with the University of Michigan - Shanghai Jiao Tong University Joint Institute, Shanghai Jiao Tong University, Shanghai 200240, China (email: yesiqi@sjtu.edu.cn, yong.long@sjtu.edu.cn).

S. Ravishankar and J. A. Fessler are with the Department of Electrical Engineering and Computer Science, University of Michigan, Ann Arbor, MI, 48109 USA (email: ravisha@umich.edu, fessler@umich.edu).

Contrary to the post-log methods, the pre-log methods work directly with the raw measurements. A robust statistical model for the pre-log raw CT measurements is the shifted-Poisson (SP) model. This model shifts the measurements by the variance of the electric readout noise. The shifted measurement has its variance equal to its mean, so that it could be approximated to be Poisson distributed. Since the shifted-Poisson model is a better approximation for CT measurement statistics compared to the Gaussian model [9], [17]–[19], and no pre-correction of the data is needed for most LDCT dose levels [9], this paper uses this SP model for LDCT image reconstruction.

There has been growing interest in improving CT image reconstruction by extracting prior knowledge from previous patient scans. Many methods have been proposed in this regard, such as prior image constrained compressed sensing methods (PICCS) [20]–[22], or the previous normal-dose scan induced nonlocal means method [23], [24]. More recently, inspired by the success of learning-based methods in image processing and computer vision, researchers have incorporated data-driven approaches along with statistical models for LDCT image reconstruction. One such approach proposed by Xu et al. [25] combined dictionary learning techniques with the PWLS method for LDCT image reconstruction. The dictionary they used was either pre-learned from a training image set (consisting of 2D images) and fixed during reconstruction, or adaptively learned while reconstructing the image. The 2D dictionary model for image patches was later extended to a 2.5D dictionary (where different dictionaries were trained from 2D image patches extracted from axial, sagittal, and coronal planes of 3D data) [26], and then to a 3D dictionary trained from 3D image patches [27]. These dictionary learning and reconstruction methods are typically computationally expensive, because they involve repeatedly optimizing NP-hard (Non-deterministic Polynomial-time hard) problems for estimating the sparse coefficients of patches. The learning of sparsifying transforms (ST) was proposed in recent works [28], [29] as a generalized analysis dictionary learning method, where the sparse coefficients are estimated directly by simple and efficient thresholding. Pre-learned square sparsifying transforms have been recently incorporated into 2D LDCT image reconstruction with both post-log Gaussian statistics [30] and pre-log SP measurement models [31]. Recent work [32] showed promise for PWLS with a union of pre-learned sparsifying transforms [33] regularization that generalizes the square sparsifying transform approach.

In addition to the dictionary learning-based approaches, some works have incorporated neural networks in CT image reconstruction. Adler and Öktem proposed a learned primal-dual reconstruction method [34], that uses convolutional neural networks (CNNs) to learn parameterized proximal operators. This method was applied to relatively simple 2D phantoms. Wu et al. [35] proposed a k-sparse autoencoder (KSAE) based regularizer for LDCT image reconstruction, where they trained three independent KSAEs from axial, sagittal and coronal slices for 3D reconstruction via artificial neural networks. Chen et al. [36] proposed to unfold the classical iterative reconstruction procedure into a CNN-based recurrent residual

network so that the original fixed regularizers and the balancing parameters within the iterative scheme can vary for each layer. The reconstruction with this network was only performed slice by slice. These methods are fully supervised learning methods requiring large datasets consisting of both undersampled images or measurements and the corresponding high-quality images. Moreover, these approaches all use post-log sinogram data, which as discussed can cause reconstruction bias.

## B. Contributions

Considering the robustness and accuracy offered by the SP statistics, and inspired by the data-driven image modeling methods not requiring paired training data or previous registered normal-dose images, here we propose a new LDCT image reconstruction method named SPULTRA that combines robust SP measurement modeling with a union of learned sparsifying transforms (ULTRA) based regularizer. Since the SP model leads to a nonconvex data-fidelity term, we design a series of quadratic surrogate functions for this term in our optimization. For each surrogate function combined with the ULTRA regularizer (a majorizer of the SPULTRA objective), we optimize it by alternating between an *image update step* and a *sparse coding and clustering step*. The image update step is performed using the relaxed linearized augmented Lagrangian method with ordered-subsets (relaxed OS-LALM) [37] and the sparse coding and clustering step is solved in closed-form. Numerical experiments compare the proposed SPULTRA method with the very recent PWLS-ULTRA scheme [32] under different incident photon intensity levels. Our results demonstrate that the proposed method avoids bias in image regions caused by the PWLS-ULTRA method, especially for low X-ray doses. At the same time, SPULTRA achieves better image reconstruction quality than PWLS-ULTRA given the same number of iterations, or alternatively, SPULTRA achieves a desired image reconstruction quality much faster than the competing PWLS-ULTRA scheme, especially for low X-ray doses.

This paper significantly extends our previous conference work [31] by incorporating the ULTRA regularizer and proposing a faster optimization procedure. Compared to the 2D LDCT results in [31], we present detailed experimental studies and comparisons for 3D LDCT reconstruction with both XCAT phantom and synthesized clinical data.

## C. Organization

The rest of this paper is organized as follows. Section II presents the proposed problem formulation for low-dose CT image reconstruction. Section III briefly reviews the ULTRA learning method and describes the proposed SPULTRA image reconstruction algorithm. Section IV presents detailed experimental results and comparisons. Section V presents conclusions.

## II. PROBLEM FORMULATION FOR SPULTRA

The goal in LDCT image reconstruction is to estimate the linear attenuation coefficients  $\mathbf{x} \in \mathbb{R}^{N_p}$  from CT measure-

ments  $\mathbf{y} \in \mathbb{R}^{N_d}$ . We propose to obtain the reconstructed image by solving a SP model-based penalized-likelihood problem:

$$\hat{\mathbf{x}} = \arg \min_{\mathbf{x} \geq 0} \Phi(\mathbf{x}), \quad \Phi(\mathbf{x}) = \mathbf{L}(\mathbf{x}) + \mathbf{R}(\mathbf{x}). \quad (\text{P0})$$

The objective function  $\Phi(\mathbf{x})$  is composed of a negative log-likelihood function  $\mathbf{L}(\mathbf{x})$  based on the SP model for the measurements, and a penalty term  $\mathbf{R}(\mathbf{x})$  that is based on the ULTRA model [32], [33]. The SP model can be described as  $Y_i \sim \text{Poisson}\{I_0 e^{-[\mathbf{A}\mathbf{x}]_i} + \sigma^2\}$ , where  $Y_i$  is the shifted quantity of the  $i$ th measurement for  $i = 1, \dots, N_d$ ,  $\sigma^2$  is the variance of the electronic noise,  $I_0$  is the incident photon count per ray from the source, and  $\mathbf{A} \in \mathbb{R}^{N_d \times N_p}$  is the CT system matrix. Denoting  $l_i(\mathbf{x}) \triangleq [\mathbf{A}\mathbf{x}]_i$  (or  $l_i$  in short), the data-fidelity term  $\mathbf{L}(\mathbf{x})$  can be written as

$$\mathbf{L}(\mathbf{x}) = \sum_{i=1}^{N_d} h_i(l_i(\mathbf{x})), \quad (1)$$

where

$$h_i(l_i) \triangleq (I_0 e^{-l_i} + \sigma^2) - Y_i \log(I_0 e^{-l_i} + \sigma^2). \quad (2)$$

The ULTRA regularizer  $\mathbf{R}(\mathbf{x})$  has the following form [32]:

$$\mathbf{R}(\mathbf{x}) \triangleq \min_{\{\mathbf{z}_j, C_k\}} \beta \sum_{k=1}^K \left\{ \sum_{j \in C_k} \tau_j \left\{ \|\Omega_k \mathbf{P}_j \mathbf{x} - \mathbf{z}_j\|_2^2 + \gamma_c^2 \|\mathbf{z}_j\|_0 \right\} \right\} \quad \text{s.t. } \{C_k\} \in \mathcal{G}, \quad (3)$$

where  $\mathcal{G}$  denotes the set consisting of all possible partitions of  $\{1, 2, \dots, N_p\}$  into  $K$  disjoint subsets,  $K$  is the number of clusters and  $C_k$  denotes the set of indices of patches belonging to the  $k$ th cluster. The operator  $\mathbf{P}_j \in \mathbb{R}^{v \times N_p}$  is the patch extraction operator that extracts the  $j$ th patch of  $v$  voxels for  $j = 1, \dots, N_p$ , from  $\mathbf{x}$ . The learned transform corresponding to the  $k$ th cluster  $\Omega_k \in \mathbb{R}^{v \times v}$  maps the patches to the transform domain. Vector  $\mathbf{z}_j \in \mathbb{R}^v$  denotes the sparse approximation of the transformed  $j$ th patch, with the parameter  $\gamma_c^2$  ( $\gamma_c > 0$ ) controlling its sparsity level. We use the  $\ell_0$  “norm” (that counts the number of nonzero elements in  $\mathbf{z}_j$ ) to enforce sparsity. The patch-based weight  $\tau_j$  is defined as  $\|\mathbf{P}_j \boldsymbol{\kappa}\|/v$  [38], [39], where  $\boldsymbol{\kappa} \in \mathbb{R}^{N_p}$  is defined to help encourage resolution uniformity as  $\kappa_j \triangleq \sqrt{\sum_{i=1}^{N_d} a_{ij} w_i / \sum_{i=1}^{N_d} a_{ij}}$  [40, eq(39)], with  $a_{ij}$  being the entries of  $\mathbf{A}$ , and  $w_i$  being the approximated inverse variance of the sinogram. To balance the data-fidelity term and the regularizer in the formulation,  $\mathbf{R}(\mathbf{x})$  is scaled by a positive parameter  $\beta$ .

### III. ALGORITHM

The proposed SPULTRA algorithm is based on a pre-learned union of sparsifying transforms. The process of learning such a union of transforms from a dataset of image patches has been detailed in [32]. The learning problem in [32] simultaneously groups the training patches into  $K$  clusters and learns a transform in each cluster along with the sparse coefficients (in the transform domain) of the patches. This learning is accomplished by an alternating algorithm (see [32]). This section focuses on describing the algorithm in the reconstruction stage for SPULTRA, i.e., for (P0).

The data-fidelity term  $\mathbf{L}(\mathbf{x})$  in (P0) is nonconvex when the electronic noise variance  $\sigma^2$  is nonzero. It is challenging to directly optimize such a logarithmic nonconvex function. We propose to iteratively design quadratic surrogate functions for this data-fidelity term  $\mathbf{L}(\mathbf{x})$ . In each iteration, we optimize the surrogate function that is a quadratic data-fidelity term together with the ULTRA regularizer using alternating minimization that alternates between an image update step and a sparse coding and clustering step that has closed-form solutions [33]. We use the relaxed OS-LALM algorithm for the image update step [37]. We perform only one alternation between the two steps for each designed surrogate function, which saves runtime and works well in practice.

#### A. Surrogate function design

We design a series of quadratic surrogate functions for  $\mathbf{L}(\mathbf{x})$  as follows:

$$\phi(\mathbf{x}; \mathbf{x}^n) = \mathbf{L}(\mathbf{x}^n) + \mathbf{d}_h(l^n) \mathbf{A}(\mathbf{x} - \mathbf{x}^n) + \frac{1}{2} (\mathbf{x} - \mathbf{x}^n)^T \mathbf{A}^T \mathbf{W}^n \mathbf{A} (\mathbf{x} - \mathbf{x}^n), \quad (4)$$

where  $(\cdot)^n$  denotes values at the  $n$ th iteration and  $\mathbf{d}_h(l^n) \in \mathbb{R}^{N_d}$  is a row vector capturing the gradient information and is defined as  $\mathbf{d}_h(l^n) \triangleq [\dot{h}_i(l_i^n)]_{i=1}^{N_d}$ . The curvatures of the  $n$ th updated parabola (surrogate) are described by  $\mathbf{W}^n \triangleq \text{diag}\{c_i(l_i^n)\}$ . In this paper, we use the optimum curvatures [41] that are defined as follows:

$$c_i(l_i^n) = \begin{cases} \left[ \frac{2 \ddot{h}_i(0) - \ddot{h}_i(l_i^n) + (l_i^n)^2 \ddot{h}_i(l_i^n)}{(l_i^n)^2} \right]_+, & l_i^n > 0 \\ [\ddot{h}_i(0)]_+, & l_i^n = 0, \end{cases} \quad (5)$$

where  $\ddot{h}_i$  is the second-order derivative, and operator  $[\cdot]_+$  sets the non-positive values to zero. In practice, we replace negative values with a small positive number so that the diagonal matrix  $\mathbf{W}^n$  is invertible. Due to numerical precision, (5) might become extremely large when  $l_i^n$  is nonzero but small. To avoid this problem, we use an upper bound of the maximum second derivative  $[\ddot{h}_i(0)]_+$  for the curvature  $c_i(l_i^n)$  when  $l_i^n > 0$  [41].

By ignoring the terms irrelevant to  $\mathbf{x}$  in (4), we get the following equivalent form of  $\phi(\mathbf{x}; \mathbf{x}^n)$ :

$$\phi(\mathbf{x}; \mathbf{x}^n) \equiv \frac{1}{2} \|\tilde{\mathbf{y}}^n - \mathbf{A}\mathbf{x}\|_{\mathbf{W}^n}^2, \quad (6)$$

where “ $\equiv$ ” means equal to within irrelevant constants of  $\mathbf{x}$ , and  $\tilde{\mathbf{y}}^n \triangleq \mathbf{A}\mathbf{x}^n - (\mathbf{W}^n)^{-1} [\mathbf{d}_h(l^n)]^T$ . The overall surrogate function at the  $n$ th iteration for the penalized-likelihood objective function  $\Phi(\mathbf{x})$  in (P0) is then

$$\Phi(\mathbf{x}; \mathbf{x}^n) = \frac{1}{2} \|\tilde{\mathbf{y}}^n - \mathbf{A}\mathbf{x}\|_{\mathbf{W}^n}^2 + \mathbf{R}(\mathbf{x}). \quad (7)$$

We optimize the surrogate function  $\Phi(\mathbf{x}; \mathbf{x}^n)$  in (7) by alternating (once) between an image update step and a sparse coding and clustering step.

#### B. Image Update Step

In the image update step, we update the image  $\mathbf{x}$  with fixed sparse codes  $\{\mathbf{z}_j\}$  and cluster assignments  $\{C_k\}$ . The relevant part of the majorizer for this step is

$$\Phi_1(\mathbf{x}; \mathbf{x}^n) = \phi(\mathbf{x}; \mathbf{x}^n) + \beta \sum_{k=1}^K \sum_{j \in C_k} \tau_j \|\Omega_k \mathbf{P}_j \mathbf{x} - \mathbf{z}_j\|_2^2. \quad (8)$$

We minimize (8) subject to the non-negativity constraint on  $\mathbf{x}$  using the relaxed OS-LALM [37] algorithm shown in Algorithm 1 (steps 7-10). The OS-LALM method uses majorizing matrices. In particular, the matrix  $\mathbf{A}^T \mathbf{W}^n \mathbf{A}$  is majorized by  $\mathbf{D}_A \triangleq \text{diag}\{|\mathbf{A}|^T |\mathbf{W}^n| |\mathbf{A}| \mathbf{1}\}$ , where  $\mathbf{1}$  denotes a vector of ones and  $|\cdot|$  computes element-wise magnitude. Denoting the regularization term in (8) as  $R_2(\mathbf{x})$ , its gradient is

$$\nabla R_2(\mathbf{x}) = 2\beta \sum_{k=1}^K \sum_{j \in C_k} \tau_j \mathbf{P}_j^T \Omega_k^T (\Omega_k \mathbf{P}_j \mathbf{x} - \mathbf{z}_j). \quad (9)$$

The Hessian of  $R_2(\mathbf{x})$  is majorized by the following diagonal matrix:

$$\mathbf{D}_R \triangleq 2\beta \left\{ \max_k \|\Omega_k^T \Omega_k\|_2 \right\} \sum_{k=1}^K \sum_{j \in C_k} \tau_j \mathbf{P}_j^T \mathbf{P}_j. \quad (10)$$

The (over-)relaxation parameter  $\alpha \in [1, 2)$  and the parameter  $\rho_t > 0$  decreases with iterations  $t$  in OS-LALM according to the following equation [37]:

$$\rho_t(\alpha) = \begin{cases} 1 & , t = 0 \\ \frac{\pi}{\alpha(t+1)} \sqrt{1 - \left(\frac{\pi}{2\alpha(t+1)}\right)^2} & , \text{otherwise.} \end{cases} \quad (11)$$

### C. Sparse Coding and Clustering Step

Here, with  $\mathbf{x}$  fixed, we jointly update the sparse codes and the cluster memberships of patches. The relevant part of the cost function for the sparse coding and clustering step is

$$\min_{\{\mathbf{z}_j, C_k\}} \sum_{k=1}^K \left\{ \sum_{j \in C_k} \tau_j \left\{ \|\Omega_k \mathbf{P}_j \mathbf{x} - \mathbf{z}_j\|_2^2 + \gamma_c^2 \|\mathbf{z}_j\|_0 \right\} \right\}. \quad (12)$$

Replacing the  $\mathbf{z}_j$ 's with their optimal values, (12) reduces to assigning the cluster for each patch as follows [32]:

$$\hat{k}_j = \underset{1 \leq k \leq K}{\text{argmin}} \|\Omega_k \mathbf{P}_j \mathbf{x} - H_{\gamma_c}(\Omega_k \mathbf{P}_j \mathbf{x})\|_2^2 + \gamma_c^2 \|H_{\gamma_c}(\Omega_k \mathbf{P}_j \mathbf{x})\|_0, \quad (13)$$

where  $H_{\gamma_c}(\cdot)$  represents a vector hard-thresholding operator that zeros out elements whose magnitudes are smaller than  $\gamma_c$ , and leaves other entries unchanged. The sparse codes  $\hat{\mathbf{z}}_j$  are computed based on the assigned clusters via hard-thresholding, i.e.,  $\hat{\mathbf{z}}_j = H_{\gamma_c}(\Omega_{\hat{k}_j} \mathbf{P}_j \mathbf{x})$ .

**Algorithm 1** illustrates the proposed optimization algorithm for Problem (P0).

### D. Computational Cost

The SPULTRA algorithm has a similar structure in each iteration as the recent PWLS-ULTRA [32], except for several initializations in the image update step. Since forward and backward projections are used to compute  $\mathbf{D}_A$  and  $\tilde{\mathbf{y}}^n$  during initialization, the image update step of SPULTRA is slightly slower than PWLS-ULTRA. In our experiments, we observed that the initializations took around 20% of the runtime in each outer iteration. However, in practice, especially for low doses, SPULTRA reconstructs images better than PWLS-ULTRA for a given number of outer iterations. Or alternatively, SPULTRA takes much fewer outer iterations (and runtime) to achieve the same image reconstruction quality as PWLS-ULTRA. These results are detailed in Sec. IV.

---

### Algorithm 1 SPULTRA Algorithm

---

#### Input:

- 1: initial image  $\hat{\mathbf{x}}^0$ ;  $\alpha = 1.999$ ;  $\rho_0 = 1$ ;
- 2: pre-computed  $\mathbf{D}_R$  according to (10);
- 3: number of outer iterations  $N$ , number of inner iterations  $P$ , and number of ordered-subsets  $M$ .

#### Output:

- reconstructed image  $\hat{\mathbf{x}}^N$ .
- for  $n = 0, 1, 2, \dots, N - 1$  do
- (1) **Image Update:** Fix  $\hat{\mathbf{z}}_j^n$  and  $\hat{C}_k^n$ ;
- 6: **Initializations:**

- 1)  $\mathbf{x}^{(0)} = \hat{\mathbf{x}}^n$ ,
- 2) Determine  $c_i(l_i^n)$  according to (5),
- 3)  $\mathbf{W}^n = \text{diag}\{c_i(l_i^n)\}$ ,
- 4)  $\mathbf{D}_A \triangleq \text{diag}\{|\mathbf{A}|^T |\mathbf{W}^n| |\mathbf{A}| \mathbf{1}\}$ ,
- 5)  $\mathbf{d}_h(l^n) = [I_0 e^{-l_i^n} (\frac{Y_i}{I_0 e^{-l_i^n} + \sigma^2} - 1)]_{i=1}^{N_d}$ ,
- 6)  $\tilde{\mathbf{y}}^n = \mathbf{A} \mathbf{x}^{(0)} - \mathbf{W}^{n-1} [\mathbf{d}_h(l^n)]^T$ ,
- 7)  $\boldsymbol{\zeta}^{(0)} = \mathbf{g}^{(0)} = M \mathbf{A}_M^T \mathbf{W}_M^n (\mathbf{A}_M \mathbf{x}^{(0)} - \tilde{\mathbf{y}}_M^n)$ ,
- 8)  $\boldsymbol{\eta}^{(0)} = \mathbf{D}_A \mathbf{x}^{(0)} - \boldsymbol{\zeta}^{(0)}$ ,
- 9) compute  $\nabla R_2(\mathbf{x})$  according to (9).

- 7: **for**  $p = 0, 1, 2, 3, \dots, P - 1$  **do**
- 8: **for**  $m = 0, 1, 2, 3, \dots, M - 1$  **do**

$t = pM + m$ ;

$$\begin{cases} \mathbf{s}^{(t+1)} = \rho_t (\mathbf{D}_A \mathbf{x}^{(t)} - \boldsymbol{\eta}^{(t)}) + (1 - \rho_t) \mathbf{g}^{(t)} \\ \mathbf{x}^{(t+1)} = [\mathbf{x}^{(t)} - (\rho_t \mathbf{D}_A + \mathbf{D}_R)^{-1} (\mathbf{s}^{(t+1)} + \nabla R_2(\mathbf{x}^{(t)}))] \\ \boldsymbol{\zeta}^{(t+1)} \triangleq M \mathbf{A}_m^T \mathbf{W}_m^n (\mathbf{A}_m \mathbf{x}^{(t+1)} - \tilde{\mathbf{y}}_m^n) \\ \mathbf{g}^{(t+1)} = \frac{\rho_t}{\rho_t + 1} (\alpha \boldsymbol{\zeta}^{(t+1)} + (1 - \alpha) \mathbf{g}^{(t)}) + \frac{1}{\rho_t + 1} \mathbf{g}^{(t)} \\ \boldsymbol{\eta}^{(t+1)} = \alpha (\mathbf{D}_A \mathbf{x}^{(t+1)} - \boldsymbol{\zeta}^{(t+1)}) + (1 - \alpha) \boldsymbol{\eta}^{(t)} \end{cases}$$

Decrease  $\rho_t$  according to (11);

- 9: **end for**
  - 10: **end for**
  - 11:  $\hat{\mathbf{x}}^{n+1} = \mathbf{x}^{(t+1)}$ ;
  - 12: (2) **Sparse Coding and Clustering:** Fix  $\hat{\mathbf{x}}^{n+1}$ , compute cluster assignments  $\hat{k}_j^{n+1}$  using (13), and sparse codes  $\hat{\mathbf{z}}_j^{n+1} = H_{\gamma}(\Omega_{\hat{k}_j^{n+1}} \mathbf{P}_j \hat{\mathbf{x}}^{n+1})$ ,  $\forall j$ .
  - 13: **end for**
- 

## IV. EXPERIMENTAL RESULTS

Here we present numerical experiments demonstrating the behavior of SPULTRA. We evaluated the proposed SPULTRA method on the XCAT phantom [42] and synthesized clinical data at multiply X-ray doses, and compared its performance with that of the state-of-the-art PWLS-ULTRA [32]. We computed the root mean square error (RMSE) and structural similarity index (SSIM) [25], [43] of images reconstructed by various methods in a region of interest (ROI). The RMSE is defined as  $\sqrt{\sum_{i \in \text{ROI}} (\hat{x}_i - x_i^*)^2 / N_{p, \text{ROI}}}$ , where  $N_{p, \text{ROI}}$  is the number of pixels in the ROI,  $\hat{\mathbf{x}}$  is the reconstructed image, and  $\mathbf{x}^*$  is the ground-truth image. We also compared to PWLS reconstruction with an edge-preserving regularizer (PWLS-EP)  $R(\mathbf{x}) = \sum_{j=1}^{N_p} \sum_{k \in N_j} \kappa_j \kappa_k \varphi(x_j - x_k)$ , where  $N_j$  represents the neighborhood of the  $j$ th pixel,  $\kappa_j$  and  $\kappa_k$  are elements of  $\boldsymbol{\kappa}$  that encourages resolution uniformity [40], and the potential

function  $\varphi(t) = \delta^2(\sqrt{1 + |t/\delta|^2} - 1)$  with  $\delta = 2 \times 10^{-4}$  mm. Both SPULTRA and PWLS-ULTRA were initialized with the result of PWLS-EP.

The SPULTRA method shifts uncorrected pre-log data by the variance of electronic noise. Such un-preprocessed pre-log data and the variance of the electronic noise on a CT scanner are proprietary to CT vendors, especially for LDCT. In our experiments, we generated pre-log data  $\hat{y}$  from the XCAT phantom as well as from a clinical image  $\tilde{x}$  reconstructed by the PWLS-ULTRA method as follows:

$$\hat{y}_i = \text{Poisson}\{I_0 e^{-[A\tilde{x}]_i}\} + \mathcal{N}\{0, \sigma^2\}, \quad (14)$$

where  $\mathcal{N}\{\mu, \sigma^2\}$  denotes a Gaussian distribution with mean  $\mu$  and variance  $\sigma^2$ . We set  $\sigma = 5$  for all the simulations [7], [32]. We refer to the pre-log data  $\hat{y}$  generated from the clinical image as *synthesized clinical data*, and the image  $\tilde{x}$  used for generating such data as the “*true*” *clinical image*.

#### A. XCAT phantom results

1) *Framework*: We pre-learned a union of 15 square transforms from  $8 \times 8 \times 8$  overlapping patches extracted from a  $420 \times 420 \times 54$  XCAT phantom with a patch stride  $2 \times 2 \times 2$ . These transforms were initialized during training [32] with 3D DCT, and the clusters were initialized randomly. We simulated

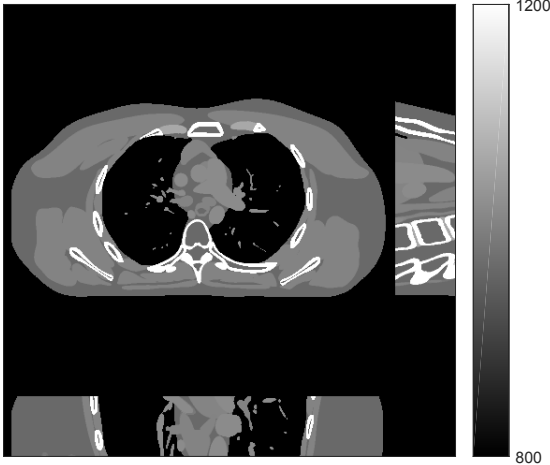


Fig. 1: Central slices of the true XCAT phantom along the axial, sagittal and coronal directions.

3D axial cone-beam scans using a  $840 \times 840 \times 96$  XCAT phantom with  $\Delta_x = \Delta_y = 0.4883$  mm and  $\Delta_z = 0.625$  mm. We generated sinograms of size  $888 \times 64 \times 984$  using GE LightSpeed cone-beam geometry corresponding to a mono-energetic source with  $I_0 = 10^4$ ,  $5 \times 10^3$ ,  $3 \times 10^3$ , and  $2 \times 10^3$  incident photons per ray and no scatter, respectively. Tab. I shows percentages of non-positive measurements under different dose levels. We set these non-positive measurements to  $1 \times 10^{-5}$  for generating the post-log sinogram that PWLS-based methods rely on. We reconstructed the 3D volume with a size of  $420 \times 420 \times 96$  at a coarser resolution of  $\Delta_x = \Delta_y = 0.9766$  mm and  $\Delta_z = 0.625$  mm. The patch size during reconstruction was  $8 \times 8 \times 8$  and the stride was  $3 \times 3 \times 3$ . For evaluating reconstruction performance, we chose a ROI that was composed of the central 64 out of 96 axial slices and a circular region in each slice containing all the

phantom structures. Fig. 1 shows the central slices of the true XCAT phantom along three directions. In the reconstruction stage of PWLS-ULTRA and SPULTRA, we used 4 iterations for the image update step, i.e.,  $P = 4$ , for a good trade-off between algorithms’ convergence and computational costs. We used 12 ordered subsets, i.e.,  $M = 12$ , to speed up the algorithm. The initial image for the ULTRA methods was reconstructed by PWLS-EP, whose regularization parameter was set empirically to ensure good reconstruction quality as  $\beta_{ep} = 2^{13}$  for all the experimented dose cases. Due to the fact that SPULTRA has a similar cost function as PWLS-ULTRA in each outer iteration, we used the same parameter settings for both methods:  $\beta = 4 \times 10^4$  and  $\gamma_c = 4 \times 10^{-4}$ , which we observed worked well for all the dose levels we tested.

TABLE I: Percentages of non-positive measurements under different dose levels for XCAT phantom simulations.

	$I_0$	$1 \times 10^4$	$5 \times 10^3$	$3 \times 10^3$	$2 \times 10^3$
Non-positive Percentage (%)		0.06	0.20	0.48	0.96

2) *Behavior of the learned ULTRA Models*: The learned union of transforms contribute to the clustering and sparsification of image patches. To illustrate the behavior of the learned transforms, we selected 3 of the 15 transforms that capture important structures/features of the reconstructed image in their clusters. Fig. 2 (first column) shows three pixel-level clusters (pixels are clustered by majority vote among patches overlapping them) for the reconstructed central axial slice. The top image only contains soft tissues, whereas the middle image shows some edges and bones in the vertical direction, and the bottom image captures some high-contrast structures. Fig. 2 (second column) shows the transforms for the corresponding classes. Each learned transform has  $512 \times 8 \times 8 \times 8$  filters, and we show the first  $8 \times 8$  slice of 256 of these filters that show gradient-like and directional features. Fig. 2 also shows the sparse coefficient images for different filters of the transforms in the third, fourth and fifth column. Each pixel value in a sparse coefficient image is obtained by applying the specific 3D filter to a 3D patch (whose top left corner is at that pixel) and hard-thresholding the result. Coefficients for patches *not belonging* to the specific cluster are set to zero (masked out). The sparse code images capture different types of image features (e.g., edges at different orientations or contrasts) depending on the filters and clusters.

3) *Numerical Results*: We compare the RMSE and the SSIM for SPULTRA with those for PWLS-EP and PWLS-ULTRA. Tab. II lists the two metrics after sufficient iterations (800 iterations) for convergence of PWLS-EP, PWLS-ULTRA, and SPULTRA, for various dose levels. The results show that SPULTRA achieves significant improvements in RMSE and SSIM in low-dose situations. Notably, compared to PWLS-ULTRA, SPULTRA further decreases the RMSE by up to 1.3 HU when  $I_0 = 3 \times 10^3$ , and by around 3.3 HU when  $I_0 = 2 \times 10^3$ .

The RMSE improvement of SPULTRA over PWLS-ULTRA can be more clearly observed from Fig. 3 that shows the

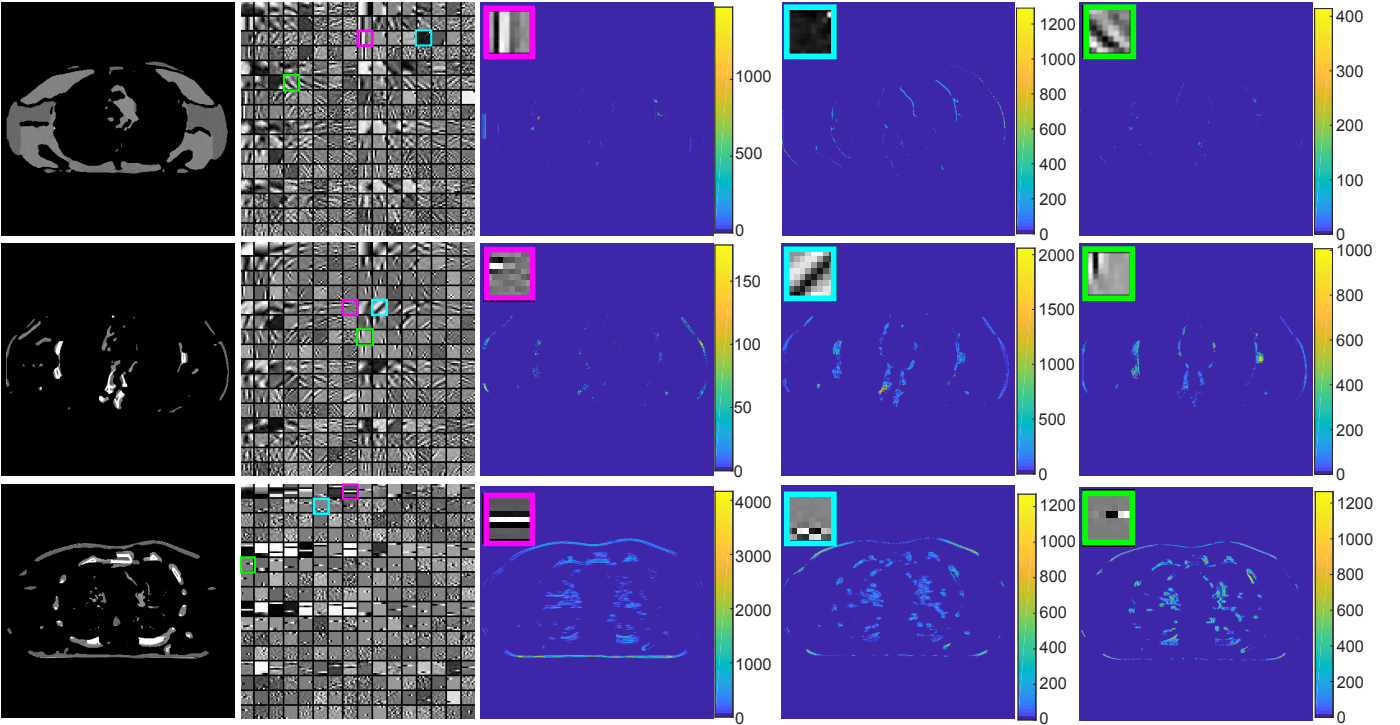


Fig. 2: Selected clustering images (first column), transforms (second column), and sparse code images (third, fourth and fifth column). The patch stride for plotting these figures is  $1 \times 1 \times 1$ .

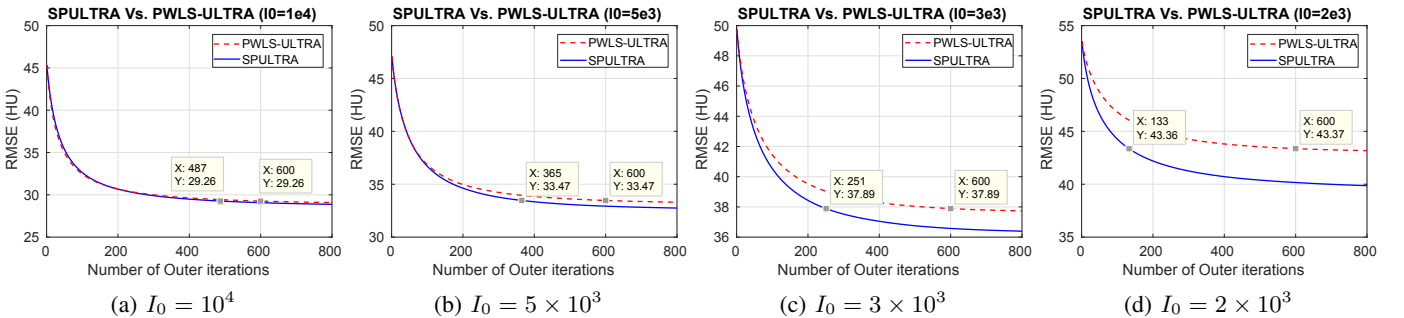


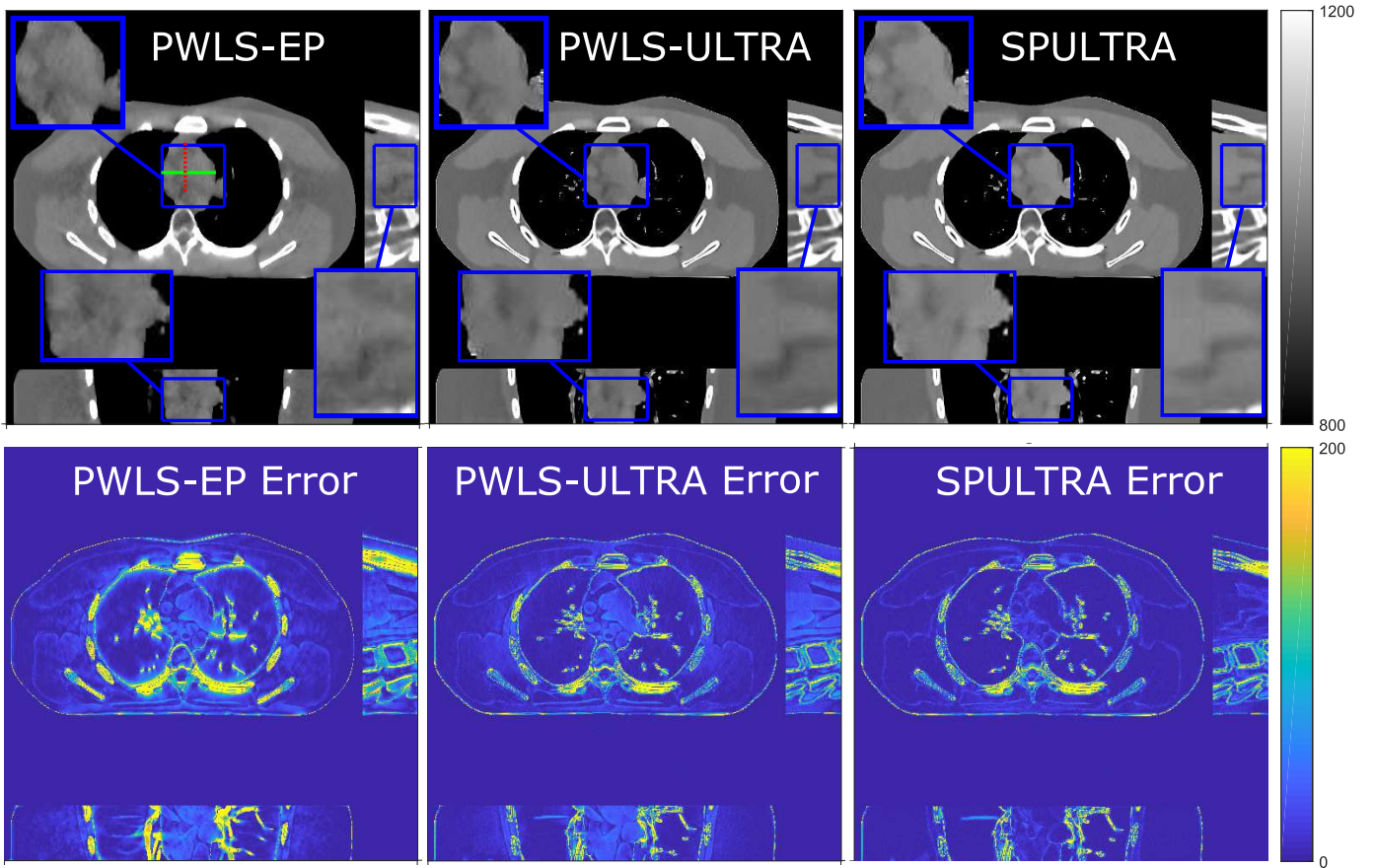
Fig. 3: RMSE comparison of SPULTRA and PWLS-ULTRA. The cursors indicate the RMSEs (Y) at specific number of outer iterations (X).

TABLE II: RMSE in HU (1st row) and SSIM (2nd row) of reconstructions at various dose levels ( $I_0$ ) using the PWLS-EP, PWLS-ULTRA, and SPULTRA methods.

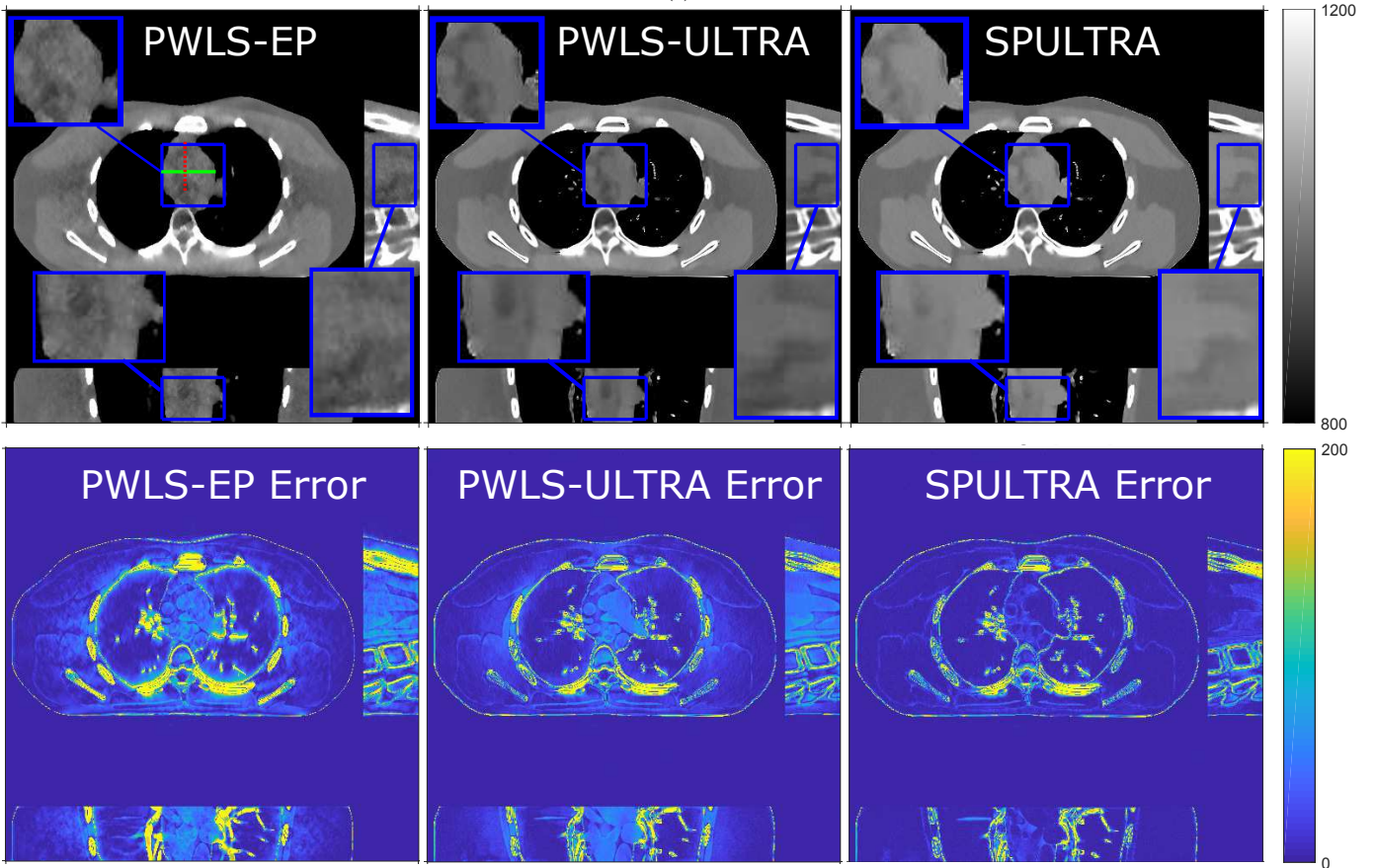
$I_0$	PWLS-EP	PWLS-ULTRA	SPULTRA
$1 \times 10^4$	45.3	29.1	<b>28.9</b>
	0.941	0.974	<b>0.974</b>
$5 \times 10^3$	47.1	33.3	<b>32.8</b>
	0.937	0.969	<b>0.970</b>
$3 \times 10^3$	49.7	37.7	<b>36.4</b>
	0.927	0.961	<b>0.963</b>
$2 \times 10^3$	53.5	43.2	<b>39.9</b>
	0.911	0.948	<b>0.956</b>

RMSE evolution with the number of outer iterations under different dose levels. At low-doses, SPULTRA decreases the RMSE more quickly (from the same initial value) and to much lower levels than PWLS-ULTRA. Fig. 3 shows that to achieve the same RMSE as PWLS-ULTRA at 600 outer iterations, SPULTRA takes 487, 365, 251 and 133 outer iterations under  $I_0 = 10^4$ ,  $5 \times 10^3$ ,  $3 \times 10^3$ , and  $2 \times 10^3$ , respectively.

4) *Computational Costs*: As discussed in Sec. III-D, SPULTRA has a similar computational cost per iteration as PWLS-ULTRA, except for computing some initializations for image update. Fig. 3 shows that the SPULTRA method requires much fewer number of outer iterations than PWLS-ULTRA to achieve the same RMSE for the reconstruction, especially at low doses. When the dose is very low, e.g., when  $I_0 = 2 \times 10^3$ , SPULTRA takes only a quarter the number of outer iterations as PWLS-ULTRA to achieve the same RMSE. Thus, the total runtime to achieve a specific reconstruction quality at low doses is typically much lower for SPULTRA than for PWLS-



(a)



(b)

Fig. 4: Comparison of reconstructions at (a)  $I_0 = 3 \times 10^3$  and (b)  $I_0 = 2 \times 10^3$  dose levels.

ULTRA. When the dose is not very low, for example when  $I_0 = 10^4$ , the SPULTRA and the PWLS-ULTRA methods have similar computational costs and runtimes. To achieve RMSE of 29.26 HU (see Fig. 3a), PWLS-ULTRA requires 600 outer iterations, while SPULTRA requires  $487 \times 120\% \approx 584$  effective outer iterations where the additional 20% runtime is associated with initializations in each SPULTRA outer iteration.

5) *Visual Results, Zoom-ins, and Image Profiles*: Fig. 4 shows the reconstructed images and the corresponding error images for PWLS-EP, PWLS-ULTRA, and SPULTRA, at  $I_0 = 3 \times 10^3$  and  $I_0 = 2 \times 10^3$ . Compared to the PWLS-EP result, both PWLS-ULTRA and SPULTRA achieved significant improvements in image quality in terms of sharper reconstructions of anatomical structures such as bones and soft tissues, and suppressing the noise. However, the PWLS-ULTRA method introduces bias in the reconstructions, which leads to larger reconstruction errors compared to the proposed SPULTRA method. In Fig. 4, we selected a 3D ROI for analysis. The central axial, sagittal, and coronal planes of the chosen ROI are marked with blue boxes with zoom-ins. Tab. III also shows the RMSE and SSIM for various methods in this ROI for different dose levels. The proposed SPULTRA clearly achieves much better RMSE and SSIM than PWLS-ULTRA.

The above advantages can be seen more clearly when observing the image profiles. Fig. 5 plots the image profiles of the three methods together with that of the ground-truth image. Fig. 4 shows the horizontal green solid line and the vertical red dashed line, whose intensities are plotted in Fig. 5. It is obvious that the profile for SPULTRA is closest to the ground-truth among the three compared methods. The gap between the profiles of the PWLS-based methods and the ground-truth shows the bias caused by the compared PWLS methods.

TABLE III: RMSE (HU) and SSIM in the selected 3D ROI in Fig. 4 at various dose levels ( $I_0$ ).

$I_0$	PWLS-EP	PWLS-ULTRA	SPULTRA
$1 \times 10^4$	39.1	28.5	<b>28.0</b>
	0.800	0.826	<b>0.829</b>
$5 \times 10^3$	43.4	34.6	<b>32.6</b>
	0.767	0.795	<b>0.804</b>
$3 \times 10^3$	50.2	43.3	<b>37.2</b>
	0.714	0.762	<b>0.776</b>
$2 \times 10^3$	60.7	55.6	<b>41.3</b>
	0.647	0.733	<b>0.752</b>

### B. Synthesized Clinical Data

1) *Framework*: We used the pre-learned union of 15 square transforms from the XCAT phantom simulations to reconstruct the synthesized helical chest scan volume of size  $420 \times 420 \times 222$  with  $\Delta_x = \Delta_y = 1.1667$  mm and  $\Delta_z = 0.625$  mm. The sinograms were of size  $888 \times 64 \times 3611$ . Since the clinical

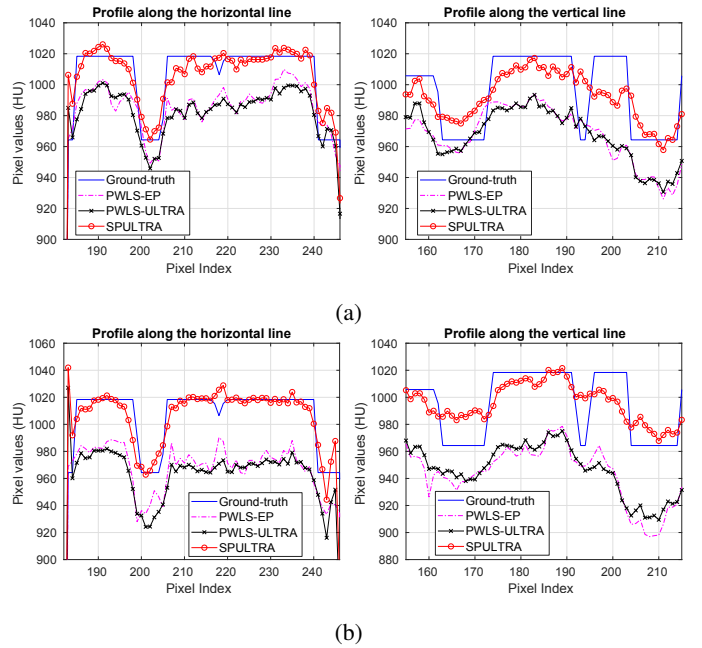


Fig. 5: Image profiles along the horizontal and vertical lines indicated in Fig. 4. (a)  $I_0 = 3 \times 10^3$ , (b)  $I_0 = 2 \times 10^3$ .

data is synthesized via the PWLS-ULTRA reconstruction, the noise model for this synthesized data is obscure, making it difficult to determine appropriate low-dose levels for such data. We tested the radiation dose of  $I_0 = 1 \times 10^4$  with an electronic noise variance the same as the XCAT phantom simulation, i.e.,  $\sigma^2 = 25$ . The percentage of non-positive pre-log measurements for the synthesized clinical data in this case was around 0.14%. Such non-positive values were replaced by  $1 \times 10^{-5}$  for PWLS-based methods. Fig. 6a shows the “true” clinical image that was reconstructed from real clinical regular-dose sinogram using the PWLS-ULTRA method. Similar to

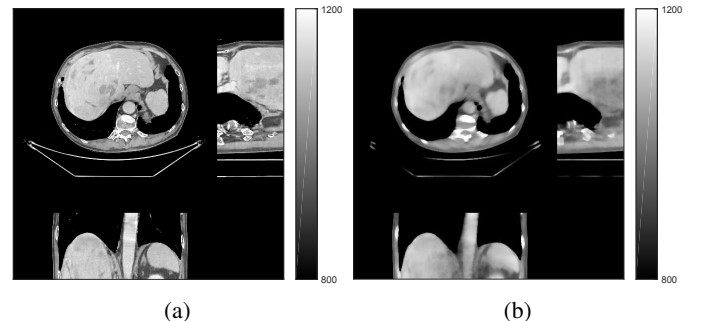


Fig. 6: (a) “true” clinical image, (b) the reconstruction of the synthesized data with PWLS-EP for  $I_0 = 1 \times 10^4$  with  $\beta_{ep} = 2^{15}$ .

the XCAT phantom simulation, the initial image for both SPULTRA and PWLS-ULTRA was a reconstruction obtained using PWLS-EP. We set the regularizer parameter  $\beta_{ep}$  for PWLS-EP as  $2^{15}$  to generate a smoother (with less noise) initial image, which led to good visual image equality for the SPULTRA and PWLS-ULTRA reconstructions. This initial image for  $I_0 = 1 \times 10^4$  is shown in Fig. 6b. The parameter  $\gamma_c$  for controlling the sparsity of SPULTRA and PWLS-ULTRA was set to be  $5 \times 10^{-4}$ , and the parameter  $\beta$  was set to be  $1.5 \times 10^4$ .

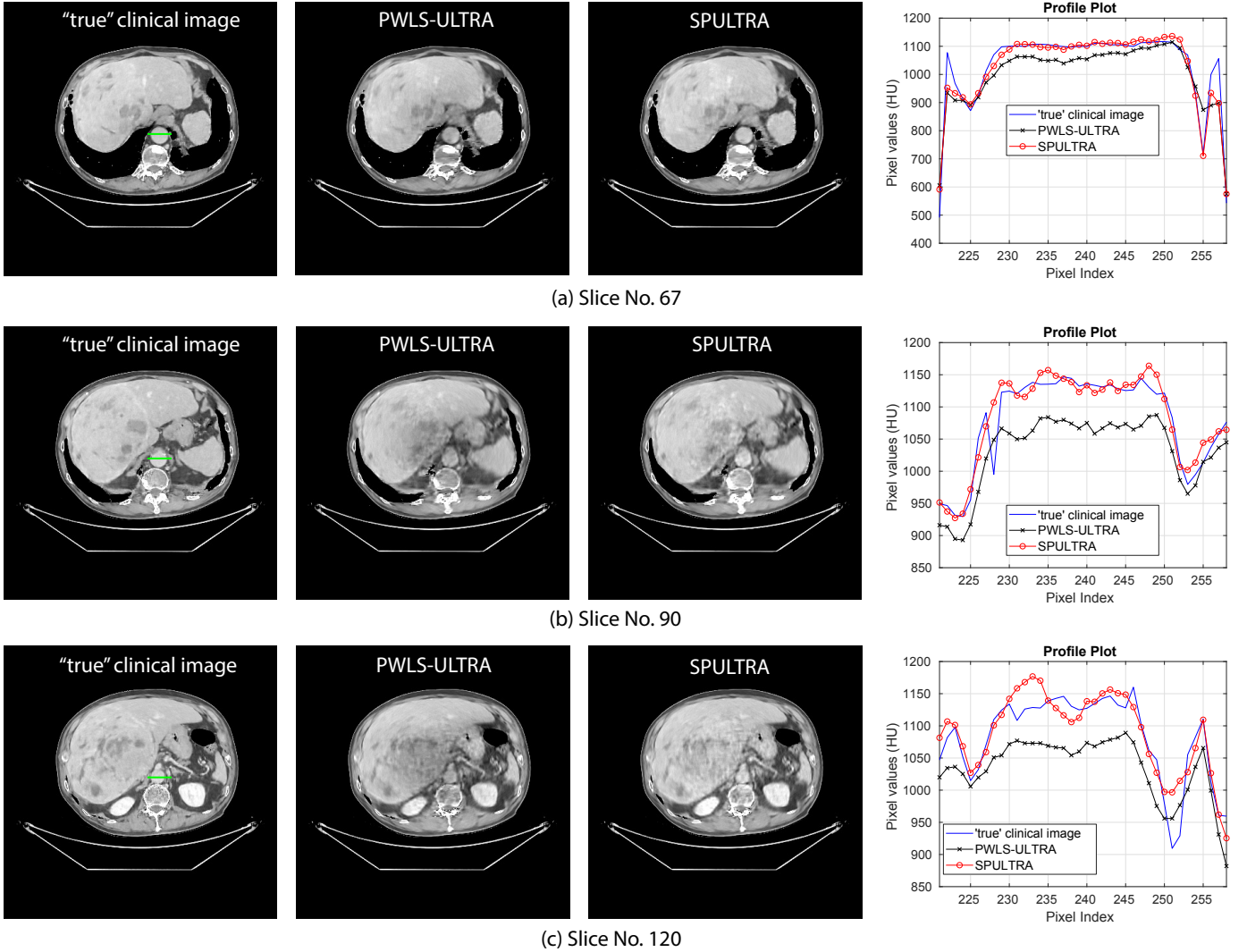


Fig. 7: Reconstructed images (columns 1 to 3) and the image profiles (the 4th column) along the green line in the “true” clinical image for the synthesized clinical data with  $I_0 = 10^4$  and  $\sigma^2 = 25$ . (a) Results for axial slice No. 67, (b) results for slice No. 90, and (c) results for slice No. 120.

2) *Reconstruction results for the synthesized clinical data:* Fig. 7 shows three axial slices from the 3D reconstructions with SPULTRA and PWLS-ULTRA at  $I_0 = 1 \times 10^4$ : the middle slice (No. 67) and two slices located farther away from the center (No. 90 and No. 120). The image profiles along a horizontal line in the displayed slices are also shown in Fig. 7. The reconstructed slices using PWLS-ULTRA appear darker around the center compared to the “true” clinical image and the reconstructions with SPULTRA. This means PWLS-ULTRA produces a strong bias in the reconstruction. The bias can be observed more clearly in the profile plots: the pixel intensities for the SPULTRA reconstruction better follow those of the “true” clinical image, while those for the PWLS-ULTRA reconstruction are much lower than the “true” values. Moreover, SPULTRA achieves sharper rising and falling edges compared to PWLS-ULTRA. In other words, SPULTRA also achieves better resolution than PWLS-ULTRA.

## V. CONCLUSIONS

This paper proposes a new LDCT reconstruction method dubbed SPULTRA that combines the shifted-Poisson statisti-

cal model with the union of learned transforms or ULTRA regularizer. To deal with the nonconvex data-fidelity term arising from the shifted-Poisson model, we iteratively designed quadratic surrogate functions for this term in the proposed algorithm. In each surrogate function update iteration, the overall cost function (i.e., majorizer) has a similar structure as in the very recent PWLS-ULTRA method, and is optimized by performing an image update step with a quadratic cost and a sparse coding and clustering step with an efficient closed-form update. We evaluated the proposed SPULTRA scheme with numerical experiments on the XCAT phantom and synthesized clinical data. SPULTRA achieved significant improvements over prior methods in terms of eliminating bias and noise in the reconstructed image while maintaining the resolution of the reconstruction under very low X-ray doses. SPULTRA was also much faster than PWLS-ULTRA in achieving a desired reconstruction quality for low-doses. We plan to investigate convergence guarantees for the proposed algorithm and incorporating variations or generalizations of the ULTRA model such as exploiting unions of overcomplete

or tall transforms, or rotationally invariant transforms in future work.

## REFERENCES

- [1] J. A. Fessler, "Statistical image reconstruction methods for transmission tomography," in *Handbook of Medical Imaging, Volume 2. Medical Image Processing and Analysis*, M. Sonka and J. Michael Fitzpatrick, Eds., pp. 1–70. SPIE, Bellingham, 2000.
- [2] J. Hsieh, "Adaptive streak artifact reduction in computed tomography resulting from excessive xray photon noise," *Med. Phys.*, vol. 25, no. 11, pp. 2139–2147, 1998.
- [3] B. R. Whiting, "Signal statistics in X-ray computed tomography," in *Medical Imaging 2002: Physics of Medical Imaging*. International Society for Optics and Photonics, 2002, vol. 4682, pp. 53–61.
- [4] I. A. Elbakri and J. A. Fessler, "Efficient and accurate likelihood for iterative image reconstruction in X-ray computed tomography," in *Medical Imaging 2003: Image Processing*. International Society for Optics and Photonics, 2003, vol. 5032, pp. 1839–1851.
- [5] L. Yu, M. Shiung, D. Jondal, and C. H. McCollough, "Development and validation of a practical lower-dose-simulation tool for optimizing computed tomography scan protocols," *J. Comput. Assist. Tomogr.*, vol. 36, no. 4, pp. 477–487, 2012.
- [6] J. Ma, Z. Liang, Y. Fan, Y. Liu, J. Huang, W. Chen, and H. Lu, "Variance analysis of X-ray CT sinograms in the presence of electronic noise background," *Med. Phys.*, vol. 39, no. 7 Part1, pp. 4051–4065, 2012.
- [7] Q. Ding, Y. Long, X. Zhang, and J. A. Fessler, "Modeling mixed Poisson-Gaussian noise in statistical image reconstruction for X-ray CT," in *Proc. 4th Intl. Mtg. on Image Formation in X-ray CT*, 2016, pp. 399–402.
- [8] J. Nuyts, B. De Man, J. A. Fessler, W. Zbijewski, and F. J. Beekman, "Modelling the physics in the iterative reconstruction for transmission computed tomography," *Phys. Med. Biol.*, vol. 58, no. 12, pp. R63, 2013.
- [9] L. Fu, T. C. Lee, S. M. Kim, A. M. Alessio, P. E. Kinahan, Z. Q. Chang, K. Sauer, M. K. Kalra, and B. De Man, "Comparison between pre-log and post-log statistical models in ultra-low-dose CT reconstruction," *IEEE Trans. Med. Imag.*, vol. 36, no. 3, pp. 707–720, 2017.
- [10] M. Beister, D. Kolditz, and W. A. Kalender, "Iterative reconstruction methods in X-ray CT," *Physica Medica: European Journal of Medical Physics*, vol. 28, no. 2, pp. 94–108, 2012.
- [11] J.-B. Thibault, K. Sauer, C. Bouman, and J. Hsieh, "A three-dimensional statistical approach to improved image quality for multi-slice helical CT," *Med. Phys.*, vol. 34, no. 11, pp. 4526–44, Nov. 2007.
- [12] D. Kim, S. Ramani, and J. A. Fessler, "Combining ordered subsets and momentum for accelerated X-ray CT image reconstruction," *IEEE Trans. Med. Imag.*, vol. 34, no. 1, pp. 167–178, Jan 2015.
- [13] I. A. Elbakri and J. A. Fessler, "Statistical image reconstruction for polyenergetic X-ray computed tomography," *IEEE Trans. Med. Imag.*, vol. 21, no. 2, pp. 89–99, 2002.
- [14] J. Wang, T. Li, H. B. Lu, and Z. R. Liang, "Penalized weighted least-squares approach to sinogram noise reduction and image reconstruction for low-dose X-ray computed tomography," *IEEE Trans. Med. Imag.*, vol. 25, no. 10, pp. 1272–1283, 2006.
- [15] J.-B. Thibault, C. A. Bouman, K. D. Sauer, and J. Hsieh, "A recursive filter for noise reduction in statistical iterative tomographic imaging," in *Proc. SPIE 6065, Computational Imaging IV*, 2006, vol. 6065, pp. 60650X–60650X–10.
- [16] J. A. Fessler, "Hybrid poisson/polynomial objective functions for tomographic image reconstruction from transmission scans," *IEEE Trans. Image Process.*, vol. 4, no. 10, pp. 1439–1450, 1995.
- [17] P. J. La Riviere, "Penalized-likelihood sinogram smoothing for low-dose CT," *Med. Phys.*, vol. 32, no. 6, pp. 1676–1683, 2005.
- [18] P. J. La Riviere, J. G. Bian, and P. A. Vargas, "Penalized-likelihood sinogram restoration for computed tomography," *IEEE Trans. Med. Imag.*, vol. 25, no. 8, pp. 1022–1036, 2006.
- [19] J. Y. Xu and B. M. W. Tsui, "Electronic noise modeling in statistical iterative reconstruction," *IEEE Trans. Image Process.*, vol. 18, no. 6, pp. 1228–1238, 2009.
- [20] G.-H. Chen, J. Tang, and S. Leng, "Prior image constrained compressed sensing (piccs): a method to accurately reconstruct dynamic CT images from highly undersampled projection data sets," *Med. Phys.*, vol. 35, no. 2, pp. 660–663, 2008.
- [21] J.C. Ramirez-Giraldo, J. Trzasko, S. Leng, L. Yu, A. Manduca, and C. H. McCollough, "Nonconvex prior image constrained compressed sensing (NCPICCS): Theory and simulations on perfusion CT," *Med. Phys.*, vol. 38, no. 4, pp. 2157–2167, 2011.
- [22] G.-H. Chen, J. Thériault-Lauzier, P. Tang, B. Nett, S. Leng, J. Zambelli, Z. Qi, N. Bevens, A. Raval, S. Reeder, et al., "Time-resolved interventional cardiac c-arm cone-beam CT: An application of the PICCS algorithm," *IEEE Trans. Med. Imag.*, vol. 31, no. 4, pp. 907–923, 2012.
- [23] J. Ma, J. Huang, Q. Feng, H. Zhang, H. Lu, Z. Liang, and W. Chen, "Low-dose computed tomography image restoration using previous normal-dose scan," *Med. Phys.*, vol. 38, no. 10, pp. 5713–5731, 2011.
- [24] H. Zhang, D. Zeng, H. Zhang, J. Wang, Z. Liang, and J. Ma, "Applications of nonlocal means algorithm in low-dose X-ray CT image processing and reconstruction: A review," *Med. Phys.*, vol. 44, no. 3, pp. 1168–1185, 2017.
- [25] Q. Xu, H. Yu, X. Mou, L. Zhang, J. Hsieh, and G. Wang, "Low-dose X-ray CT reconstruction via dictionary learning," *IEEE Trans. Med. Imag.*, vol. 31, no. 9, pp. 1682–97, Sept. 2012.
- [26] J. Luo, H. Eri, A. Can, S. Ramani, L. Fu, and B. De Man, "2.5 D dictionary learning based computed tomography reconstruction," in *SPIE Defense+ Security*. pp. 98470L–98470L–12, International Society for Optics and Photonics.
- [27] J. Liu, Y. Hu, J. Yang, Y. Chen, H. Shu, L. Luo, Q. Feng, Z. Gui, and G. Coatrieux, "3D feature constrained reconstruction for low-dose CT imaging," *IEEE Trans. Circuits Syst. Video Technol.*, vol. 28, no. 5, pp. 1232–1247, May 2018.
- [28] S. Ravishanker and Y. Bresler, "Learning sparsifying transforms," *IEEE Trans. Signal Process.*, vol. 61, no. 5, pp. 1072–1086, 2013.
- [29] S. Ravishanker and Y. Bresler, " $\ell_0$  sparsifying transform learning with efficient optimal updates and convergence guarantees," *IEEE Trans. Signal Process.*, vol. 63, no. 9, pp. 2389–2404, 2015.
- [30] X. Zheng, Z. Lu, S. Ravishanker, Y. Long, and J. A. Fessler, "Low dose CT image reconstruction with learned sparsifying transform," in *Proc. IEEE Wkshp. Image, Video, Multidim. Signal Process. (IVMSP)*, 2016, pp. 1–5.
- [31] S. Ye, S. Ravishanker, Y. Long, and J. A. Fessler, "Adaptive sparse modeling and shifted-Poisson likelihood based approach for low-dose CT image reconstruction," in *Proc. IEEE Wkshp. Machine Learning for Signal Proc.*, 2017, pp. 1–6.
- [32] X. Zheng, S. Ravishanker, Y. Long, and J. A. Fessler, "PWLS-ULTRA: An efficient clustering and learning-based approach for low-dose 3D CT image reconstruction," *IEEE Trans. Med. Imag.*, vol. 37, no. 6, pp. 1498–1510, 2018.
- [33] B. Wen, S. Ravishanker, and Y. Bresler, "Structured overcomplete sparsifying transform learning with convergence guarantees and applications," *Intl. J. Comp. Vision*, vol. 114, no. 2-3, pp. 137–167, 2015.
- [34] J. Adler and O. Öktem, "Learned primal-dual reconstruction," *IEEE Trans. Med. Imag.*, vol. 37, no. 6, pp. 1322–1332, 2018.
- [35] D. Wu, K. Kim, G. El Fakhri, and Q. Li, "Iterative low-dose CT reconstruction with priors trained by artificial neural network," *IEEE Trans. Med. Imag.*, vol. 36, no. 12, pp. 2479–2486, 2017.
- [36] H. Chen, Y. Zhang, Y. Chen, J. Zhang, W. Zhang, H. Sun, Y. Lv, P. Liao, J. Zhou, and G. Wang, "LEARN: Learned experts assessment-based reconstruction network for sparse-data CT," *IEEE Trans. Med. Imag.*, vol. 37, no. 6, pp. 1333–1347, June 2018.
- [37] H. Nien and J. A. Fessler, "Relaxed linearized algorithms for faster X-ray CT image reconstruction," *IEEE Trans. Med. Imag.*, vol. 35, no. 4, pp. 1090–1098, Apr. 2016.
- [38] J. A. Fessler and W. L. Rogers, "Spatial resolution properties of penalized-likelihood image reconstruction: space-invariant tomographs," *IEEE Trans. Image Process.*, vol. 5, no. 9, pp. 1346–1358, Sept 1996.
- [39] I. Y. Chun, X. Zheng, Y. Long, and J. A. Fessler, "Sparse-view X-ray CT reconstruction using  $\ell_1$  regularization with learned sparsifying transform," in *Proc. Intl. Mtg. on Fully 3D Image Recon. in Rad. and Nuc. Med*, 2017, pp. 115–9.
- [40] J. H. Cho and J. A. Fessler, "Regularization designs for uniform spatial resolution and noise properties in statistical image reconstruction for 3-D X-ray CT," *IEEE Trans. Med. Imag.*, vol. 34, no. 2, pp. 678–689, 2015.
- [41] H. Erdogan and J. A. Fessler, "Monotonic algorithms for transmission tomography," *IEEE Trans. Med. Imag.*, vol. 18, no. 9, pp. 801–814, 1999.
- [42] W. P. Segars, M. Mahesh, T. J. Beck, E. C. Frey, and B. M. W. Tsui, "Realistic CT simulation using the 4D XCAT phantom," *Med. Phys.*, vol. 35, no. 8, pp. 3800–8, Aug. 2008.
- [43] Y. Zhang, X. Mou, G. Wang, and H. Yu, "Tensor-based dictionary learning for spectral CT reconstruction," *IEEE Trans. Med. Imag.*, vol. 36, no. 1, pp. 142–154, 2017.